Journal of Materials Chemistry C



View Article Online PAPER



Near-infrared emission, energy transfer, and mechanisms of Mn²⁺ and Cr³⁺ Co-doped lead-free Cs2AgInCl6 double perovskites†

Daiwen Chen,‡a Cu Wu,‡a Huayuan Li,a Liya Zhou, 📵 Peican Chen,a Qi Pang, 📵 *a Xinguo Zhang b and Jin Zhong Zhang c

Doping metal ions into lead halide perovskites is a promising method to regulate their structural stability and optical properties. In this work, Mn^{2+}/Cr^{3+} codoped $Cs_2AgInCl_6$ double perovskite single crystals (DPSCs) were synthesized using a programmed cooling hydrothermal method. Upon light excitation at 350 nm, the co-doped CAIC:Mn²⁺,Cr³⁺ DPSC samples exhibit two photoluminescence (PL) bands with a wide emission switch ranging from orange to NIR. The photoluminescence quantum yield (PLQY) of the NIR emission can be increased to 49.30% by varying the concentration of dopant ions. The high PLQY is attributed to the energy transfer (ET) from selftrapped excitons (STEs) to Mn²⁺ and Cr³⁺ dopant ions. The presence of ET was confirmed by analyzing time-resolved photoluminescence (TRPL) and temperature-dependent PL. Moreover, we determine the ET pathway from STE to Mn²⁺ ions at low temperatures using temperature-dependent PL spectra. The emission colors of CAIC:Mn²⁺,Cr³⁺ DPSCs can be continuously tuned from yellow to orange by controlling temperature. This ET-induced dual emission seems to be governed by thermal activation. A model is proposed to explain the efficient ET processes from the host DPSCs to Mn^{2+} and Cr^{3+} dopants, as well as possible ET processes from Mn^{2+} to Cr3+ ion centers.

Received 9th July 2023, Accepted 17th August 2023

DOI: 10.1039/d3tc02410e

rsc.li/materials-c

1. Introduction

Lead halide perovskites have shown great application potential in light-emitting diodes, solar cells, photovoltaics, and other optoelectronic devices due to their unique optoelectronic properties. 1-6 Lead-based perovskites have a near-unity photoluminescence (PL) quantum yield (QY), but the toxicity of lead (Pb) and low stability in the natural environment limit their further commercialization.^{7,8} In this regard, double perovskites, represented by Cs2AgInCl6, with unique structures and excellent optronic properties, are emerging. Pristine and modified Cs2AgInCl6 is non-toxic and has excellent light and thermal stability and is a promising alternative to lead-based

perovskites.^{9,10} Therefore, researchers propose expanding application potentials of such materials through ion doping and alloying. 11-14 Dopants introduce additional radiative decay channels, and new emission bands appear. 15 Xia et al. synthesized the Cs₂AgInCl₆:Bi nanocrystals (NCs) with a PLQY as high as 11.4%.16 In addition, they successfully synthesized Cs2AgInCl₆ co-doped with Tb³⁺ and Bi³⁺, achieving tunable emission from green to orange.17 Nag et al. adopted Bi-Er and Bi-Yb codoped CAIC to increase the NIR emission intensity circa 45 and 27 times, compared to Cs₂AgInCl₆:Er and Cs₂AgInCl₆:Yb.¹⁰ Locardi et al. obtained a broad spectrum white PL (PLQY ~ $1.6 \pm 1\%$) nanocrystals by doping Mn ions.¹⁴

In recent years, the light source of broadband near-infrared (NIR) has received increasing attention because of its essential roles in biological imaging, non-destructive testing, and night vision. 18-24 However, most studies of luminescent double perovskites (DPs) have focused on visible light emission and narrowband NIR emission, with broadband NIR emission much less studied. 10,25,26 Therefore, broadband NIR-emitting lead-free metal halide perovskites are of great interest. Currently, the most popular methods to broaden the emission band of NIR emission are multisite occupation and an impurity doping strategy. Multisite occupation refers to provision of two or more octahedral cation sites for Cr³⁺ ions within the matrix.

^a Guangxi Key Laboratory of Petrochemical Resource Processing and Process Intensification Technology, School of Chemistry and Chemical Engineering, Guangxi University, Nanning 530004, Guangxi, P. R. China. E-mail: pqigx@163.com

^b School of Pharmaceutical Sciences, Southern Medical University, Guangzhou

^c Department of Chemistry and Biochemistry, University of California, Santa Cruz, California 95064, USA

[†] Electronic supplementary information (ESI) available. See DOI: https://doi.org/

[‡] Daiwen Chen and Chu Wu contributed equally to this work.

This method has been confirmed to be effective in Li_{1.6}Zn_{1.6}S $n_{2.8}O_8$:Cr³⁺ (FWHM = 190 nm)^{27,28} and La₂MgZrO₆ (FWHM = 210 nm).²⁹ The typical impurity doping strategy was multidoping with Nd, Yb, Er and Tm; Cs2AgInCl6:Bi/Ln showed an ultra-broadband continuous emission spectrum with a FWHM of about 365 nm.30 Guo et al. successfully synthesized a broadband NIR luminescent phosphor CaZrGeO:Cr with a FWHM of 160 nm. 31 However, co-doping multiple Ln 3+ ions may produce nonradiative migration in a sole host. Cr3+ has been shown to produce broadband NIR luminescence emission of 650-1350 nm in the octahedron with weak crystal field interaction. 18-20 Therefore, Cr3+ is an excellent near-infrared sensitizer. To date, the synthesized method and the NIR luminescence of Cr3+ doped DPs remained to be further improved. 32,33 Cs₂AgInCl₆:Cr³⁺ obtained by the traditional high-temperature solid-state reaction has wide band nearinfrared emission characteristics with a PLQY of 22.03%.34 The Cs₂Ag_{1-x}Na_xInCl₆:Cr³⁺ nanocrystals were prepared by Xia et al. with a PLQY of 19.7%.35 Therefore, finding an effective method to trigger the sensitization of Cr³⁺ in DPs to enhance the NIR emission performance is highly desired and significant. Codoping of perovskites with two different ions can provide more synthesis flexibility and optical tunability but has been less explored. 33,36-38 Mn²⁺ ions are one of the most studied dopants, and when Mn2+ ions enter the strong crystal field, their emission is located in the yellow or red region.³⁹ Mn²⁺ ions are mostly used as luminescence centers, so their role as a sensitizer is often overlooked.

This study synthesized Mn²⁺ and Cr³⁺ co-doped CAIC DPSCs using a programmed cooling hydrothermal method. The Mn²⁺ and Cr3+ co-doped CAIC DPSCs exhibit a unique two-band emission covering visible and NIR spectral regions. Steadystate and time-resolved photoluminescence (TRPL) spectroscopies reveal an effective ET process from the host to Mn²⁺ and Cr³⁺ dopants and a possible ET process from Mn²⁺ to Cr³⁺ ion

Results and discussion

2.1 Structural and electronic properties

X-Ray diffraction (XRD) patterns of CAIC, CAIC:Mn²⁺ and CAIC: Mn²⁺, Cr³⁺ DPSCs are shown in Fig. 1a. All samples can be well assigned to the CAIC phase with an $Fm\bar{3}m$ space group. No noticeable impurity detected was observed by XRD analysis of all the DPSC products, suggesting that Mn²⁺ doping or Mn²⁺/ Cr3+ codoping does not affect the structure of CAIC. Fig. 1b exhibits the schematics of CAIC: Mn2+, Cr3+ DPSC structure in polyhedral representation. The addition of Mn²⁺ does not cause any shift in the XRD peak position, probably due to the small amount of Mn²⁺ in the product (Fig. S1, ESI†).⁴⁰ Moreover, the (220) plane diffraction peak of DPSCs slightly shifts toward a higher angle with an increase in the Cr3+ feed ratio (Fig. S2, ESI†). The shift of the diffraction peaks is consistent with the phenomenon of lattice contraction, which also indicates that the successfully doped Cr³⁺ ions.^{34,41} Due to their identical

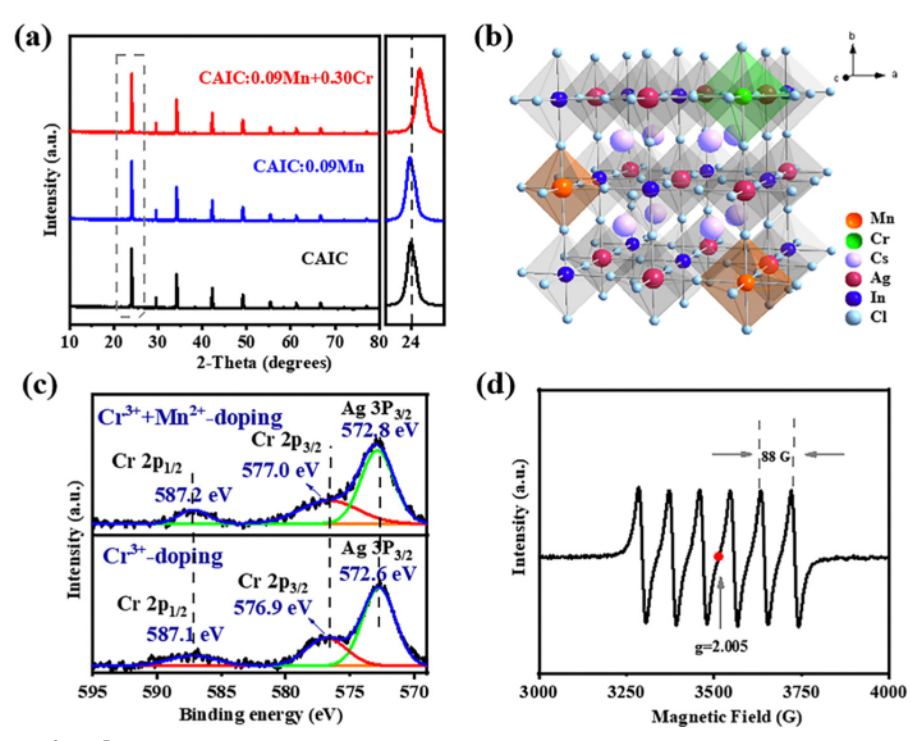


Fig. 1 (a) XRD patterns of Mn²⁺, Cr³⁺ doped CAIC DPSCs and (220) locally enlarged view of crystal plane. (b) Crystal structure schematic illustration of Mn²⁺, Cr³⁺ doped CAIC DPSCs. (c) XPS spectra of CAIC: 0.09Mn²⁺, 0.30Cr³⁺ DPSCs for Cr 2P peaks. The spectra are calibrated using C 1s peak. (d) EPR spectrum for the Mn²⁺, Cr³⁺ doped CAIC DPSCs.

ionic radius and oxidation state, Mn^{2+} (r = 0.83, CN = 6) and Cr^{3+} ions (r = 0.62, CN = 6) are proposed to substitute In^{3+} ions (r = 0.8, CN = 6), generating $[\text{CrCl}_6]^{3-}$ and $[\text{MnCl}_6]^{4-}$ octahedrons, respectively.34

Fig. S3a-f (ESI†) and Fig. 1c show the XPS spectra of the codoped DPSCs. All elements in CAIC: Mn²⁺, Cr³⁺can be found. The co-doped samples show Mn 2p and Cr 2P peaks, indicating the co-existence of Mn²⁺ and Cr³⁺ ions. In the XPS narrow spectrum of Cr 2p, the peaks of 587.2 eV and 577.0 eV can be attributed to Cr 2p_{1/2} and Cr 2p_{3/2}, while no peaks about Cr⁴⁺ are found, confirming that Cr is still in the +3 valence state. 42 The peak of 572.8 eV is attributed to Ag $3p_{3/2}$. The binding energy of Cr 2p matches that of Cr3+ ions in the octahedron reported in previous studies. 43,44 In addition, after doping Mn2+ and Cr3+ ions, all the Cl 2p, Cs 3d, and In 4f peaks shift to higher energy indicating stronger In-Cl interactions in CAIC: Mn²⁺, Cr³⁺. ⁴⁵ The EPR spectrum of CAIC: Mn²⁺, Cr³⁺ DPSCs is shown in Fig. 1d. The spectrum shows the characteristic gfactor equal 2.005, there are six nuclear-electron hyperfine splitting peaks, and the average splitting constant is 88 G. This indicates that Mn²⁺ ions are successfully inserted into the octahedral coordination environment of the perovskite lattice.46 The measurements of electron paramagnetic resonance (EPR) and X-ray photoelectron spectroscopy (XPS) further indicate the successful doping of Mn²⁺ and Cr³⁺ ions.

Scanning electron microscopy (SEM), inductively coupled plasma-atomic emission spectroscopy (ICP-AES) and energy dispersive spectroscopy (EDS) studies were conducted to determine the morphology and elemental content of the samples. Fig. S4 (ESI†) presents the SEM images of DPSCs (a), photographs of DPSCs obtained via an optical microscope (b), and the simulated crystal faces for one crystal particle (c) showing that the synthesized single crystal presents a regular octahedron with a millimeter-sized edge length of about 1.0 mm, with its characteristic purple transparent color indicating increased absorption of visible light compared to CAIC. 47 The EDS spectra results confirm that the Cs, In, Ag, Cl, Cr and Mn elements are uniformly distributed in the whole DPSCs (Fig. S5, ESI†). The doping concentrations of all ions in the DPSCs were determined by ICP-AES. The results are shown in Table S1 (ESI†). The actual doping concentration is small and lower than the initial dosage in the synthesis.

2.2 Optical properties

The PL spectra and TRPL decay profiles of CAIC: Mn2+ DPSCs are shown in Fig. 2(a) and (b). Under 350 nm excitation, the sample doped with Mn2+ has a strong luminescence emission centered at 635 nm, and the full-width-at-half-maximum (FWHM) is 86 nm. The luminescence intensity increased monotonously with the increase of Mn2+ content from 0.01 to 0.09 mmol. The best sample (x = 0.09) has a PLQY of about 2.45%. The emission intensity is maximum when Mn²⁺ doping amount is about 9%, and further increasing the Mn²⁺ content may reduce the luminescence intensity due to Mn-Cl-Mn exchange interactions, which is similar to the previous literature.48 TRPL spectra show that all decay curves conform to a double exponential function. The average lifetime of the best sample (CAIC: 0.09Mn²⁺) is 370 μs. The millisecond-level lifetime is composed of the Mn^{2+} d-d transitions of ${}^4T_1-{}^6A_1$ which is consistent with an existing report.⁴⁶

The spectral overlap between the excitation peak of Cr^{3+} and the emission peak of Mn²⁺ in singly doped CAIC is shown in Fig. 2(c). There is an overlap between the excitation peaks of Cr³⁺ and the emission peaks of Mn²⁺. It can be inferred that energy transfer (ET) from Mn²⁺ → Cr³⁺ exists in CAIC: Mn²⁺, Cr3+. This means that the emission of Cr3+ can be effectively improved and regulated by using Mn²⁺ ions as the sensitizer. Therefore, we added different amounts of Cr3+ into CAIC: 0.09Mn²⁺ and performed optical characterization.

Fig. 3a shows the diffuse reflectance spectra (DRS) of the samples. The undoped CAIC DPSCs show an absorption band around 350 nm, and no absorption peak was observed in the range of 400 to 900 nm. The bandgap of CAIC is about 3.2 eV by the Kubelka-Munk model (inset of Fig. 3a) which is similar to previous literature reports.^{9,47} In contrast, Mn²⁺-doped CAIC DPSCs have a broad absorption band centered at 600 nm, and the bandgap does not change, suggesting the successful doping of Mn²⁺ into the perovskite lattice. Cr³⁺-doped CAIC DPSCs show two broad absorption bands with maxima at around 580 nm and 830 nm, which can be attributed to the Cr3+ d-d transitions of ${}^{4}A_{2} \rightarrow {}^{4}T_{1}$ and ${}^{4}A_{2} \rightarrow {}^{4}T_{2}$. The dominant 350 nm band is caused by an electronic transition from the valence band to the conduction band in the CAIC host. The Co-doped sample exhibits both the features of the single-doped Mn sample and the single-doped Cr sample, showing the successful

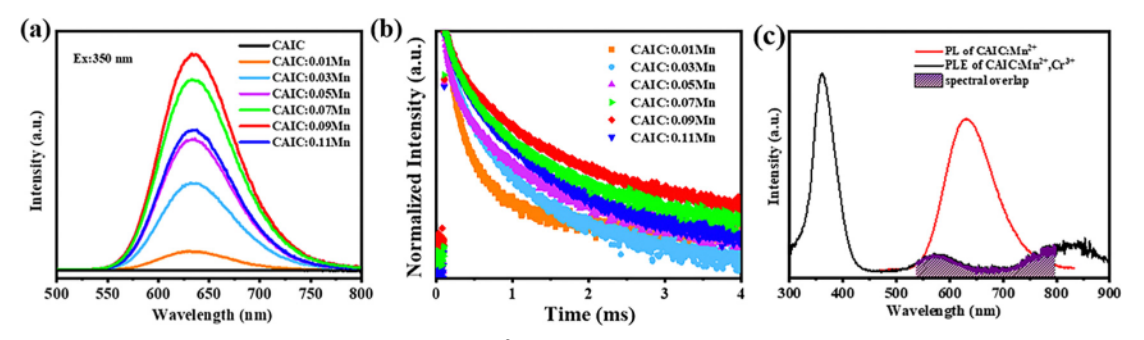


Fig. 2 The PL spectra (a) and the TRPL decay profiles of CAIC: xMn²⁺ DPSCs (b). (c) The spectral overlapping between the PL spectrum of CAIC: Mn²⁺ and the excitation band of CAIC: Mn²⁺, Cr³⁺.

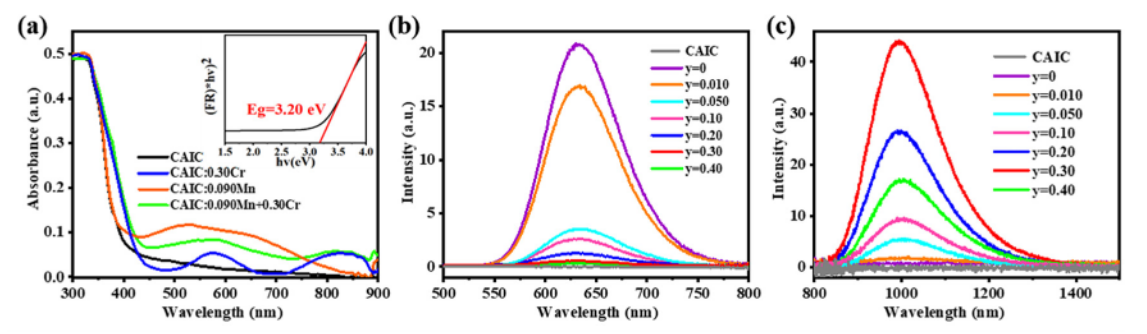


Fig. 3 (a) DRS of CAIC: Mn^{2+} , Cr^{3+} . The inset shows the DR spectrum of the CAIC DPSC host with $[F(R) \times hv]^2$ as a function of photon energy, for determining the band gap energy. (b) and (c) PL spectra of CAIC: 0.09Mn²⁺, yCr³⁺ in the range of (b) 500-800 nm and (c) 800-1500 nm at 350 nm

co-doping of the two ions into the lattice and the addition of new absorption channels.

Fig. 3(b) and (c) show the visible and near-infrared spectra of CAIC: 0.09Mn^{2+} , $y \text{Cr}^{3+}$ (y = 0 - 0.4) excited by 350 nm light at room temperature, corresponding to the emission of Mn²⁺ and Cr³⁺, respectively. All the samples are excited at 350 nm, with the emission wavelength range extending from 550 nm to 750 nm, and the maximum emission at 635 nm, which can be attributed to the spin forbidden d-d transitions of ${}^{4}\Gamma_{1}$ - ${}^{6}A_{1}$, and isolated Mn²⁺ ions doped in CAIC. 48 Simultaneously, a broadband NIR emission is shown at 800-1400 nm. This range spans near-infrared-I (NIR-I) biowindow (750-1000 nm) and near-infrared-II (NIR-II) biowindow (1000-1350 nm) with a FWHM of 188 nm, and PLQY of 49.30% (Fig. S6, ESI†). Interestingly, by introducing the Cr3+ions, the Mn2+ PL intensity decreases, the Cr3+ NIR emission at 1000 nm appears and intensity simultaneously increases with the Cr3+ doping concentration then decreases after reaching the maximum value (y = 0.30) due to concentration quenching. Fig. S7 (ESI†) shows PL excitation (PLE) spectra of CAIC: Mn²⁺, Cr³⁺DPSCs with the emission wavelength at 1000 nm. Obviously, the energy transfer (ET) process leads to the decrease of Mn²⁺ PL intensity and the increase of Cr3+ PL intensity (the detailed mechanism of ET will be discussed below). As shown in Fig. S8 (ESI†), the excitation wavelength varies between 300 and 550 nm. The PL spectral intensity varies with different excitation wavelengths, but the shape remains the same, indicating

that the broad emission band in the 800-1400 nm range is caused by the same spin-permitted transition of ${}^{4}T_{2} \rightarrow {}^{4}A_{2}$ of Cr^{3+} .

The spectral range of the NIR emission of CAIC: Mn²⁺, Cr³⁺ DPSCs (FWHM = 188 nm) is much broader than other NIR phosphors, such as LaMgGa₁₁O₁₉:Cr³⁺(FWHM = 138 nm) and $MgTa_2O_6$: Cr^{3+} (FWHM = 140 nm). 49,50 Cr^{3+} ions exhibit broadband emission and longer emission wavelength in the weaker crystal field environment. The classical Tanabe-Sugano theory can be used to clarify the octahedral crystal field splitting in which Cr³⁺ is situated. Fig. S9 (ESI†) shows the Tanabe-Sugano diagram of the Cr3+ ions in octahedral coordination.51 The value of Dq/B can be used to judge the crystal field intensity. The calculation method of the values of *Dq* and *B* is in the ESI.† The values of Dq and B are ~ 1204 and 533 cm⁻¹, which results in a Dq/B value of 2.25 (Fig. S9, ESI†). When Dq/B < 2.30, Cr^{3+} ions are in a weak crystal field environment, which will result in a broadband emission of ${}^{4}T_{2} \rightarrow {}^{4}A_{2}$ transition. 35,52 This result shows that the Cr³⁺ ions in CAIC: Mn²⁺, Cr³⁺ host are in a weak crystal field, and thus form a broadband near-infrared emission.

To better study the process of ET, the time-resolved PL (TRPL) spectra were measured for all samples, and the results are shown in Fig. 4a-c and Tables S2, S3 (ESI†). The decay curves of all Mn²⁺ ions can be fitted by formula (1):⁵³

$$I_t = I_0 + A_1 \exp\left(\frac{-t}{1}\right) + A_2 \exp\left(\frac{-t}{2}\right) \tag{1}$$

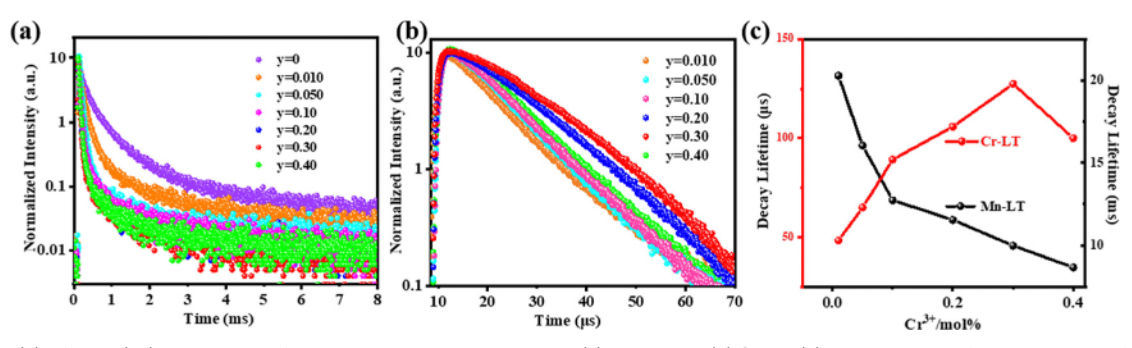


Fig. 4 (a) and (b) Lifetime (LT) decay curves for the samples when monitoring (a) Mn-PL and (b) Cr-PL. (c) The summary of the average LTs for Mn (black), and Cr (red) PLs.

where I_t is the PL intensity and I_0 is the initial PL intensity at t = 0, A_1 and A_2 are constants, and τ_1 and τ_2 are the decay times of the fast and slow exponential components, respectively. The average lifetime (τ_{ave}) can be calculated using eqn (2):

$$\tau_{\text{ave}} = \frac{A_1 \tau_1^2 + A_2 \tau_2^2}{A_1 \tau_1 + A_2 \tau_2} \tag{2}$$

As the doping amount of Cr^{3+} increases, the decay time of Mn^{2+} decreases monotonically, which strongly proves the energy transfer of $Mn^{2+} \rightarrow Cr^{3+}$ (Fig. 4a and Table S2, ESI†). In addition, decay curves of all Cr^{3+} ions conform to a single exponential function (Fig. 4b), and the lifetime gradually increases with the increase of the Cr^{3+} doping amount, further indicating that the improved energy transfer from Mn^{2+} to Cr^{3+} ions promotes the decay of Mn^{2+} , and the related trend graph is shown in Fig. 4c.

The energy transfer efficiency η_T of $\text{Mn}^{2+} \to \text{Cr}^{3+}$ ions can be determined using eqn (3).⁵⁴

$$\eta_{\rm T} = 1 - \frac{\tau}{\tau_0} \tag{3}$$

where τ is the decay time of Mn²⁺ in the presence of Cr³⁺, and τ_0 is the decay time of Mn²⁺ in the absence of Cr³⁺. When $y=0.010,\,0.050,\,0.10,\,0.20,\,0.30,\,$ and 0.40, the η_T value is estimated to be 64.5, 74, 85, 89, 90, and 91%, respectively. Obviously, as the Cr³⁺ doping concentration increases, the effective energy transfer increases. The calculated relationship between the Cr³⁺ concentration and the calculated energy transfer efficiency is shown in Fig. 5a. As the Cr³⁺ concentration increased from 0.2 to 0.4, η_T values keep largely invariable (from 89% to 91%), indicating that the energy transfer was close to saturation. The results show that the energy transfer process of Mn²⁺ \rightarrow Cr³⁺ is very efficient in the CAIC host.

The mechanism of the resonant ET process from the sensitizer to the activator is divided into electric multipolar interaction and exchange interaction. The critical distance ($R_{\rm c}$) is a key parameter that determines the type of resonant ET process. ⁵⁵ When $R_{\rm c} > 5$ Å, electric multipolar interaction plays

a dominant role in the ET process. Conversely, the ET process is dominated by exchange interaction. The calculation of $R_{\rm c}$ was publicized as follows. ⁵⁶

$$R_{\rm c} = 2 \left[\frac{3V}{4\Pi x_{\rm c} N} \right]^{1/3} \tag{4}$$

where V is the volume of the unit cell, x_c and N are the critical concentration of doped ions, and the number of host cations in the unit cell, respectively. Finally, the R_c value is estimated to be 15.39 Å. This value was much greater than 5 Å, confirming that the ET process from $Mn^{2+} \rightarrow Cr^{3+}$ in the CAIC host is dominated by the electric multipolar interaction. The Dexter's formula can be used to determine the type of multipolar interaction in CAIC: $0.09Mn^{2+}$, γCr^{3+} :⁵⁵

$$\frac{\eta_{s0}}{\eta_s} \propto C^{\alpha/3} \tag{5}$$

where C is the total concentration of the Mn²⁺ and Cr³⁺ ions. η_{80} is the PLQY of Mn²⁺ ions in the absence of Cr³⁺ ions, and η_{8} is the PLQY of Mn²⁺ ions in the presence of Cr³⁺ ions. The α value can be used to distinguish quadrupole–quadrupole, dipole–dipole and dipole–quadrupole interactions. It is usually to calculate I_{80}/I_{8} (I represent the luminescence intensity) to replace η_{80}/η_{8} . Therefore, Formula (6) can approximate the ET process of multipolar interactions. ⁵⁴

$$\frac{I_{\rm s0}}{I_{\rm s}} \propto C^{\alpha/3} \tag{6}$$

According to the above equation, Fig. 5b shows the relationship between $C^{\alpha/3}$ and I_{s0}/I_s . It is confirmed that the ET of Mn²⁺ \rightarrow Cr³⁺ is carried out through the quadrupole–quadrupole interaction mechanism.

2.3 Temperature-dependent PL properties

To study the thermal quenching behavior of the samples, the variable temperature luminescence spectra of CAIC: 0.09Mn^{2+} , 0.30Cr^{3+} sample was tested from 120 to 400 K. Fig. 6a shows the temperature-dependent PL (500–800 nm) properties of CAIC: 0.09Mn^{2+} , 0.30Cr^{3+} . When the temperature (T) is higher than

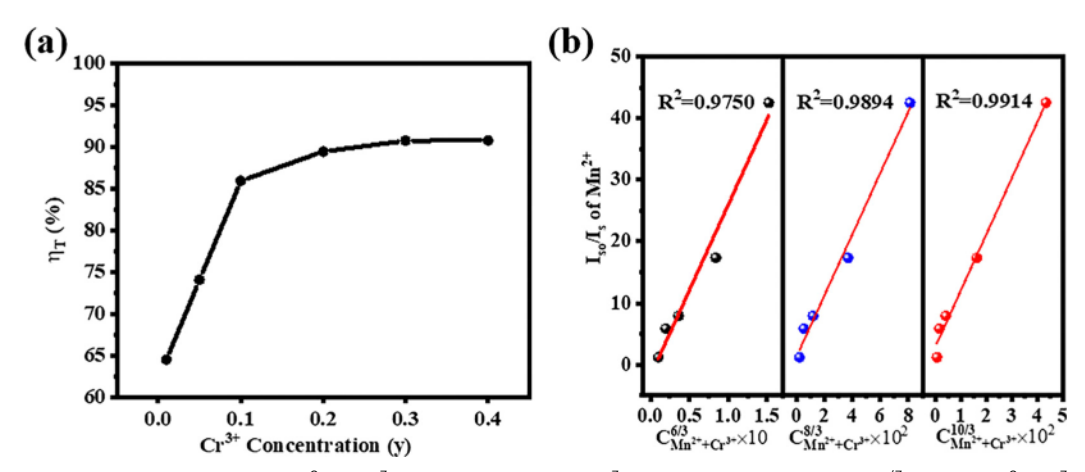


Fig. 5 (a) The energy transfer efficiency from Mn^{2+} to Cr^{3+} ions as a function of Cr^{3+} concentration. (b) $I_{s0}/I_s - C^{z/3}$ plots of Mn^{2+} , Cr^{3+} co-doped CAIC PCSCs.

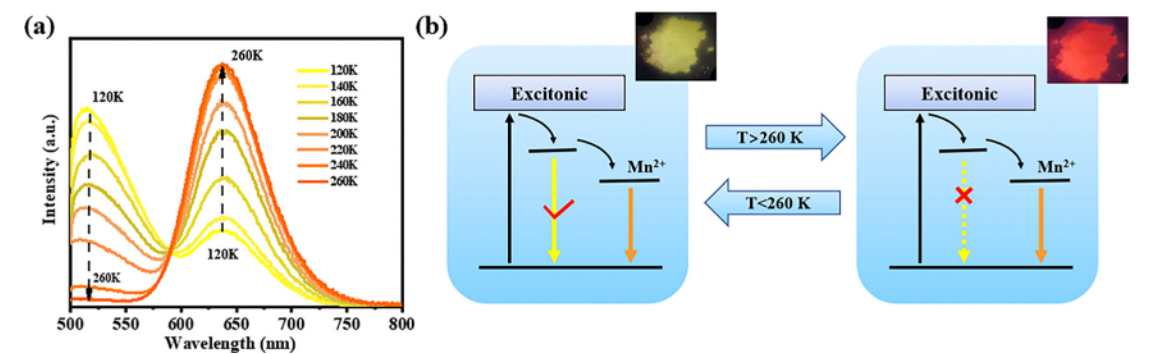


Fig. 6 (a) Temperature-dependent emission spectra of CAIC: $0.09Mn^{2+}$, $0.30Cr^{3+}$ DPSCs under 350 nm excitation in the temperature range of 120-400 K with a temperature interval of 20 K. (b) Schematic of the dual emission energy transfer controlled by thermal activation. Insets: Sample photos taken by a visible camera at different temperatures.

260 K, the visible emission is led by Mn²⁺ emission, and the emission of self-trapping excitons (STE) is completely suppressed. However, when T < 260 K, the PL from STE is observed in addition to Mn²⁺ emission. The results suggest that the ET process from STE → Mn²⁺ is inhibited at lower temperatures. However, at higher temperatures, ET from STE \rightarrow Mn²⁺ is more efficient. As a result, the Mn²⁺ emission intensity increases gradually with the increase in temperature. The ET-induced dual emission seems to be governed by thermal activation. This results in a change in the color of the CAIC: 0.09Mn²⁺, 0.30Cr³⁺ from bright yellow to orange as the temperature was increased from 80 K to 260 K. 57,58 Fig. 6b shows a schematic of the ET-induced dual emission controlled by thermal activation.

Fig. 7a shows the temperature-dependent PL (800-1400 nm) spectra of CAIC: 0.09Mn²⁺, 0.30Cr³⁺. Fig. 7b shows the trend of the PL intensity of two emission peaks at 630 nm and 1000 nm as a function of temperature under a 350 nm excitation. The temperature variation trend of the two peaks is consistent between 120 K and 400 K. This confirms the presence of ET from STE to Mn²⁺ and Cr³⁺ dopant ions. The relationship between 1/kT and $\ln (I_0/I_t - 1)$ of CAIC: 0.09Mn²⁺, 0.30Cr³⁺ is shown in Fig. 7c. Two distinct different linear processes at high and low temperatures indicate that they are two distinct thermal processes. The Arrhenius equation is usually used to

describe the exciton binding energy of thermal quenching:59

$$I_{t} = \frac{I_{0}}{1 + C_{\text{exp}}\left(\frac{-E_{a}}{kT}\right)} \tag{7}$$

Formula (8) represents the Arrhenius equation for multiple thermal processes:60

$$I_{t} = \frac{I_{0}}{1 + C_{\exp}\left(\frac{-\Delta E_{1}}{kT}\right) + C_{2\exp}\left(\frac{-\Delta E_{2}}{kT}\right)}$$
(8)

where I_t and I_0 are the initial PL intensity and the PL intensity at a given temperature, k represents the Boltzmann constant, C is also a constant independent of temperature, and ΔE_1 and ΔE_2 are exciton binding energy for high and low-temperature processes, respectively. The fitting results are shown in Fig. 7c. The calculated results of ΔE_1 , and ΔE_2 are 650 meV and -0.5 meV, respectively. Negative exciton binding energy at low temperatures indicates a complex pathway. This complex process is mainly caused by the ET of STE to Mn2+ and Cr3+ ions. Meanwhile, we measured and calculated the exciton binding energy of CAIC: Cr³⁺ DPSCs (Fig. S10, ESI[†]). The exciton binding energy of CAIC: Cr3+ and CAIC: Mn2+, Cr3+ were calculated to be 215 meV and 650 meV based on the temperature-dependent PL spectra, respectively, indicating that the co-doped samples

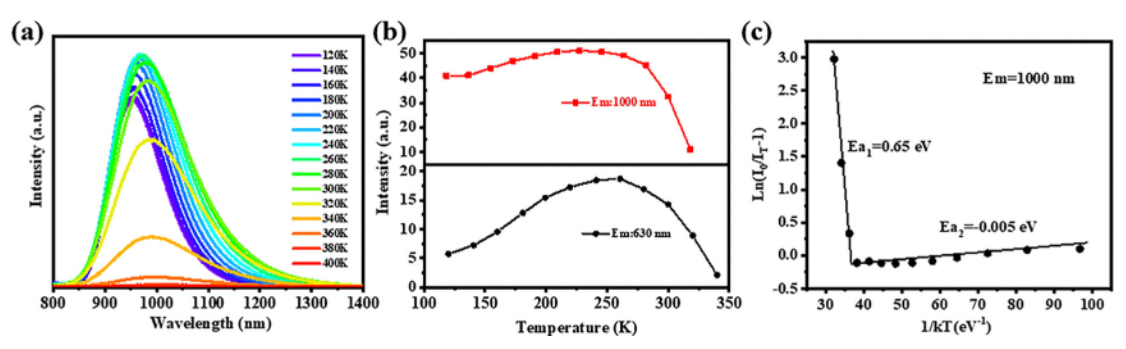


Fig. 7 (a) Temperature-dependent PL spectra of CAIC: $0.09Mn^{2+}$, $0.30Cr^{3+}$ DPSCs under 350 nm excitation in the temperature range of 120–400 K with a temperature interval of 20 K. (b) Temperature-dependent relative integrated intensities. (c) Plot of $Ln(l_0/l_{t-1})$ versus 1/kT of the temperaturedependent spectrum of CAIC: 0.09Mn²⁺, 0.30Cr³⁺ DPSCs when excited at 350 nm.

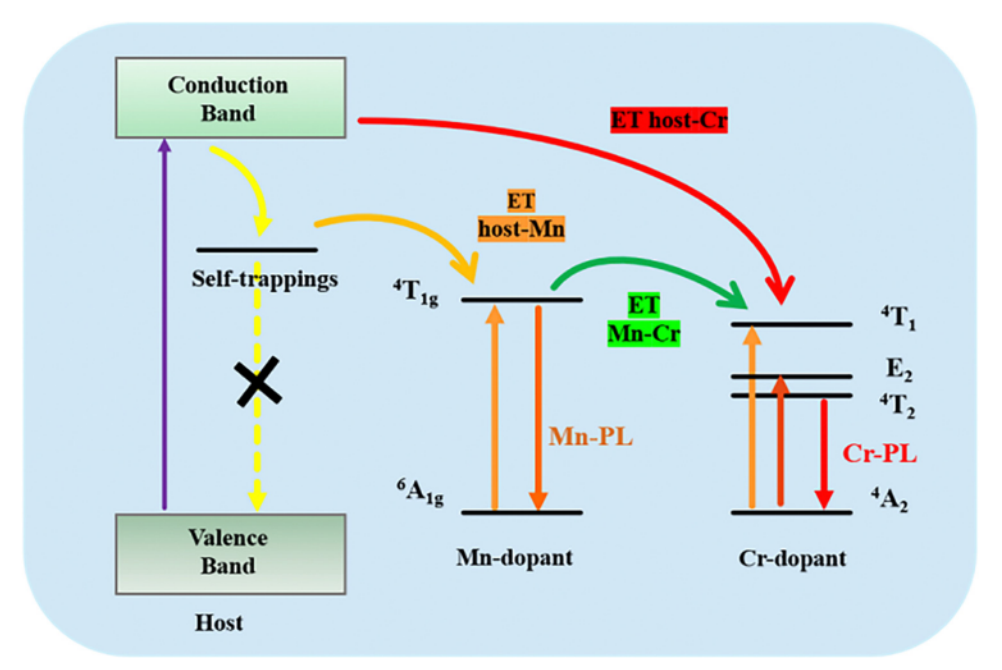


Fig. 8 Schematic of the proposed energy transfer (ET) processes in the Mn²⁺ and Cr³⁺ codoped CAIC DPSCs.

have better thermal stability. We measured the light stability of CAIC:Cr3+ and CAIC: Mn2+, Cr3+ samples under ultraviolet radiation for 3 h (Fig. S11, ESI†). The PL intensity of the CAIC:Cr³⁺ sample decreased by 25%, while the co-doped sample CAIC: Mn²⁺, Cr³⁺ decreased by only 20%. The difference in light and thermal stability between CAIC:Cr3+ and CAIC: Mn2+, Cr³⁺ may be related to electron-phonon coupling. We can calculate the coupling effect between electrons and phonons

according to eqn (9) by fitting the relationship between FWHM of the PL spectrum and temperature.⁶¹

$$FWHM = 2.36\sqrt{S}\hbar\omega\sqrt{\coth\left(\frac{\hbar\omega}{2kT}\right)}$$
 (9)

where S is the Huang-Rhys parameter, $\hbar\omega$ stands for the phonon frequency, T is the Kelvin temperature, and k is the

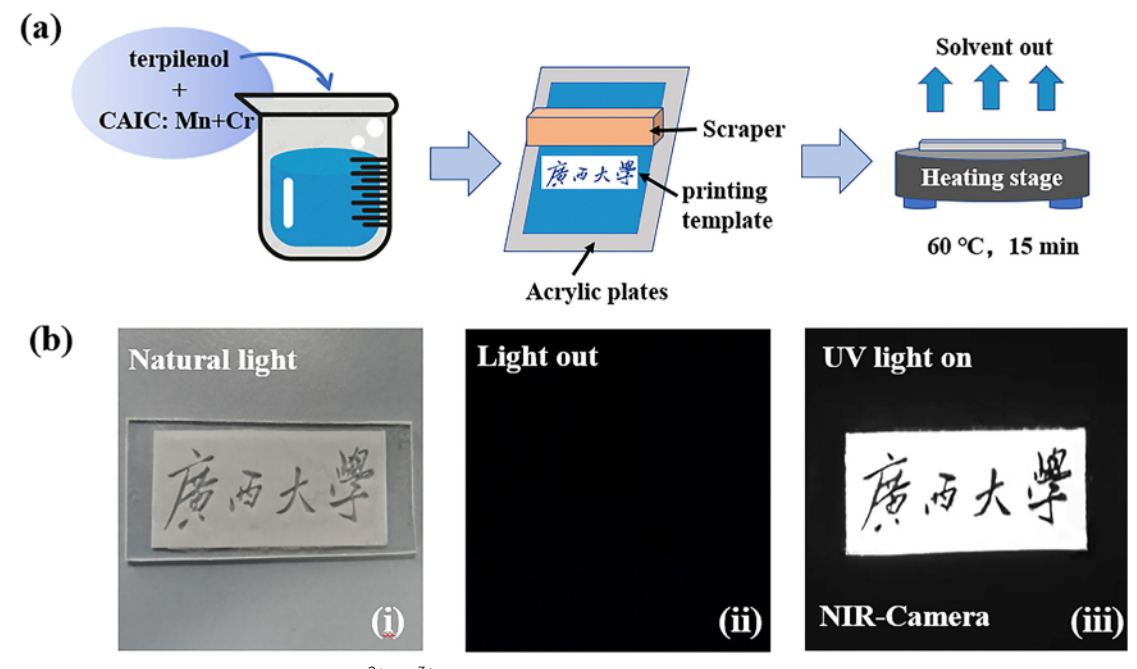


Fig. 9 (a) Scheme of the fabrication of the CAIC: Mn²⁺, Cr³⁺ DPSCs film by using a screen printing method. (b) Photographs under natural light captured by a visible camera (i) and in the dark captured by a NIR camera under UV excitation light when it is off (ii) and on (iii).

Boltzmann constant. The fitting results of the relationship between FWHM² and 2kT are depicted in Fig. S12 (ESI†). The $\hbar\omega$ and S for CAIC: ${\rm Cr}^{3+}$ are 0.0305 eV and 3.16, and those for CAIC: Mn²⁺, Cr³⁺ are 0.0295 eV and 3.12. Combined with the calculated exciton binding energy analysis, we believe that the CAIC: Mn²⁺, Cr³⁺ DPSC samples have higher exciton binding energy and such relatively lower phonon disturbance, all of which indicate that the addition of Mn²⁺ ions significantly increases the radiation recombination of Cr³⁺ ions. ⁶² Therefore, the co-doping of Mn2+ and Cr3+ effectively inhibits the strong exciton-phonon interaction and greatly increases the probability of radiation transition.

2.4 Luminescence mechanism

To help explain the results obtained, we propose a possible mechanism that describes the photoexcitation, ET, and radiative pathways for the Mn²⁺/Cr³⁺ codoped CAIC DPSCs, as shown in Fig. 8. After the UV light excitation, the electrons are excited from the ground state into the excited state of the CAIC host, which is then trapped in the STE state through non-radiative relaxation. Upon doping Mn²⁺ ions, a portion of excited electrons can transfer energy to the excited state (${}^{4}T_{1g}$) of the Mn²⁺ through the resonant Dexter-type energy transfer process.⁶³ When codoped with Cr3+, energy transfer can occur directly from the CAIC host to Cr³⁺ or indirectly from the ⁴T_{1g} state of Mn^{2+} to the 4T_1 state of Cr^{3+} , leading to increased Cr^{3+} PLQY when codoped with Mn²⁺.45,64

2.5 NIR fluorescent sign applications

Based on the excellent luminous performance and stability, we demonstrated the application of the DPSCs for luminescent pattern formation. We mixed the CAIC: Mn²⁺, Cr³⁺ DPSCs with terpineol to get desired patterns through screen printing (Fig. 9a). Fig. 9b shows a photon of the pattern taken with a normal camera in light (Fig. 9bi) and in darkness (Fig. 9bii). When the 365 nm UV is turned on, the pattern can be seen by the NIR camera (Fig. 9biii). The results suggest that CAIC: Mn²⁺, Cr³⁺ DPSCs are promising for NIR fluorescent signs and night vision as an environmentally friendly perovskite.

3. Conclusions

In summary, Mn²⁺ and Cr³⁺ ions were successfully doped into Cs₂AgInCl₆ DPSCs prepared via a modified facile hydrothermal method, and the resulting samples exhibit tunable emission from orange to NIR depending on the concentration of doped ions. At the optimal concentration of dopant ions, the PLQY of NIR emission reaches 49.30%. The high PLQY is attributed to the ET from STE to Mn²⁺ and Cr³⁺ dopant ions. The presence of ET was confirmed by the analysis of TRPL and temperaturedependent PL. Furthermore, the feasibility of using the sample for NIR high-resolution images and night vision was successfully demonstrated. This work shows that ionic doping is an effective strategy for the NIR emission tuning of Cr3+-doped DPSCs and will provide guidance for the application expansion of metal halide perovskite in the NIR region.

Conflicts of interest

There are no conflicts to declare.

Acknowledgements

This work was supported by the National Natural Science Foundation of China (grant no. 21965003) and the Opening Project of Guangxi Key Laboratory of Petrochemical Resource Processing and Process Intensification Technology (grant no. 2022K008). JZZ acknowledges the US NSF (CHE-2203633) for financial support.

References

- 1 Q. A. Akkerman, G. Raino, M. V. Kovalenko and L. Manna, Nat. Mater., 2018, 17, 394-405.
- 2 P. V. Kamat, J. Bisquert and J. Buriak, ACS Energy Lett., 2017, 2, 904-905.
- 3 F. Zhou, Z. Li, H. Chen, Q. Wang, L. Ding and Z. Jin, Nano Energy, 2020, 73, 104757.
- 4 M. Li and Z. Xia, Chem. Soc. Rev., 2021, 50, 2626-2662.
- 5 C. Wang, D. Han, J. Wang, Y. Yang, X. Liu, S. Huang, X. Zhang, S. Chang, K. Wu and H. Zhong, Nat. Commun., 2020, 11, 6428.
- 6 X. Li, D. Yu, J. Chen, Y. Wang, F. Cao, Y. Wei, Y. Wu, L. Wang, Y. Zhu, Z. Sun, J. Ji, Y. Shen, H. Sun and H. Zeng, ACS Nano, 2017, 11, 2015-2023.
- 7 L. Protesescu, S. Yakunin, M. I. Bodnarchuk, F. Krieg, R. Caputo, C. H. Hendon, R. X. Yang, A. Walsh and M. V. Kovalenko, Nano Lett., 2015, 15, 3692-3696.
- 8 M. A. Becker, R. Vaxenburg, G. Nedelcu, P. C. Sercel, A. Shabaev, M. J. Mehl, J. G. Michopoulos, S. G. Lambrakos, N. Bernstein, J. L. Lyons, T. Stoferle, R. F. Mahrt, M. V. Kovalenko, D. J. Norris, G. Raino and A. L. Efros, *Nature*, 2018, 553, 189-193.
- 9 J. Luo, S. Li, H. Wu, Y. Zhou, Y. Li, J. Liu, J. Li, K. Li, F. Yi, G. Niu and J. Tang, ACS Photonics, 2017, 5, 398-405.
- 10 H. Arfin, J. Kaur, T. Sheikh, S. Chakraborty and A. Nag, Chem. Int. Ed., 2020, 59, 11307-11311.
- 11 Q. Hu, G. Niu, Z. Zheng, S. Li, Y. Zhang, H. Song, T. Zhai and J. Tang, Small, 2019, 15, e1903496.
- 12 F. Ji, F. Wang, L. Kobera, S. Abbrent, J. Brus, W. Ning and F. Gao, Chem. Sci., 2021, 12, 1730-1735.
- 13 Q. Liao, J. Chen, L. Zhou, T. Wei, L. Zhang, D. Chen, F. Huang, Q. Pang and J. Z. Zhang, J. Phys. Chem. Lett., 2020, 11, 8392-8398.
- 14 F. Locardi, M. Cirignano, D. Baranov, Z. Dang, M. Prato, F. Drago, M. Ferretti, V. Pinchetti, M. Fanciulli, S. Brovelli, L. De Trizio and L. Manna, J. Am. Chem. Soc., 2018, 140, 12989-12995.

- 15 Y. Gao, C. Yan, X. Peng, W. Li, J. Cao, Q. Wang, X. Zeng, X. Fu and W. Yang, Nanoscale, 2021, 13, 18010-18031.
- 16 Y. Liu, Y. Jing, J. Zhao, Q. Liu and Z. Xia, Chem. Mater., 2019, 31, 3333-3339.
- 17 Y. Liu, X. Rong, M. Li, M. S. Molokeev, J. Zhao and Z. Xia, Angew. Chem., Int. Ed., 2020, 59, 11634-11640.
- 18 M. Mao, T. Zhou, H. Zeng, L. Wang, F. Huang, X. Tang and R.-J. Xie, J. Mater. Chem. C, 2019, 1981–1988, DOI: 10.1039/ c9tc05775g.
- 19 D. Dai, Z. Wang, Z. Xing, X. Li, C. Liu, L. Zhang, Z. Yang and P. Li, J. Alloys Compd., 2019, 806, 926-938.
- 20 Z. Pan, Y. Y. Lu and F. Liu, Nat. Mater., 2011, 11, 58-63.
- 21 J. Wang, J. Li, J. Yu, H. Zhang and B. Zhang, ACS Nano, 2018, 12, 4246-4258.
- 22 M. Ye, Z. Gao, Z. Li, Y. Yuan and T. Yue, Food Chem., 2016, 190, 701-708.
- 23 J. Qiao, G. Zhou, Y. Zhou, Q. Zhang and Z. Xia, Nat. Commun., 2019, 10, 5267.
- 24 Z. Li, Y. Zhang, X. Wu, L. Huang, D. Li, W. Fan and G. Han, J. Am. Chem. Soc., 2015, 137, 5304-5307.
- 25 Y. Mahor, W. J. Mir and A. Nag, J. Phy. Chem. C, 2019, 123, 15787-15793.
- 26 R. Wu, P. Han, D. Zheng, J. Zhang, S. Yang, Y. Zhao, X. Miao and K. Han, Laser Photonics Rev., 2021, 15, 2100218.
- 27 J. A. Lai, J. Zhou, Z. Long, J. Qiu, D. Zhou, Y. Yang, K. Zhang, W. Shen and Q. Wang, Mater. Des., 2020, 192, 2200965.
- 28 X. Z. Jinmeng Xiang, X. Zhao, Z. Wu, C. Chen, X. Zhou and C. Guo, Laser Photonics Rev., 2023, 17, 2200965.
- 29 H. Zeng, T. Zhou, L. Wang and R.-J. Xie, Chem. Mater., 2019, 31, 5245-5253.
- 30 S. Jin, R. Li, H. Huang, N. Jiang, J. Lin, S. Wang, Y. Zheng, X. Chen and D. Chen, Light: Sci. Appl., 2022, 11, 52.
- 31 J. Xiang, J. Zheng, X. Zhao, X. Zhou, C. Chen, M. Jin and C. Guo, Mater. Chem. Front., 2022, 6, 440-449.
- 32 D. Zhou, D. Liu, G. Pan, X. Chen, D. Li, W. Xu, X. Bai and H. Song, Adv. Mater., 2017, 29, 1704149.
- 33 D. Zhou, R. Sun, W. Xu, N. Ding, D. Li, X. Chen, G. Pan, X. Bai and H. J. N. L. Song, Nano Lett., 2019, 19, 6904-6913.
- 34 F. Zhao, Z. Song, J. Zhao and Q. Liu, Inorg. Chem. Front., 2019, 6, 3621-3628.
- 35 A. Zhang, Y. Liu, G. Liu and Z. Xia, Chem. Mater., 2022, 34, 3006-3012.
- 36 F. Meinardi, Q. A. Akkerman, F. Bruni, S. Park, M. Mauri, Z. Dang, L. Manna and S. Brovelli, ACS Nano Energy Lett., 2017, 2, 2368-2377.
- 37 T. A. Cohen, T. J. Milstein, D. M. Kroupa, J. D. MacKenzie, C. K. Luscombe and D. R. Gamelin, J. Mater. Chem. A, 2019, 7, 9279-9288.
- 38 F. Meinardi, F. Bruni and S. J. N. R. M. Brovelli, Nat. Rev. Mater., 2017, 2, 1-9.
- 39 W. Liu, Q. Lin, H. Li, K. Wu, I. Robel, J. M. Pietryga and V. I. Klimov, J. Am. Chem. Soc., 2016, 138, 14954-14961.
- 40 K. Nila Nandha and A. Nag, Chem. Commun., 2018, 54, 5205–5208.

- 41 D. Chen, X. Zhang, J. Wei, L. Zhou, P. Chen, Q. Pang and J. Z. Zhang, Inorg. Chem. Front., 2022, 9, 4695-4704.
- 42 X. Duan, J. Liu, Y. Wu, F. Yu and X. Wang, J. Lumin., 2014, 153, 361-368.
- 43 W. Zhou, J. Luo, J. Fan, H. Pan, S. Zeng, L. Zhou, Q. Pang and X. Zhang, Ceram. Int., 2021, 47(18), 25343-25349.
- 44 A. M. Salvi, J. E. Castle, J. F. Watts and E. Desimoni, Appl. Surf. Sci., 1995, 90, 333-341.
- 45 T. Cai, J. Wang, W. Li, K. Hills-Kimball, H. Yang, Y. Nagaoka, Y. Yuan, R. Zia and O. Chen, Adv. Sci., 2020, 7, 2001317.
- 46 L. Chen, W. Yang, H. Fu, W. Liu, G. Shao, B. Tang and J. Zheng, J. Mater. Sci., 2021, 56, 8048-8059.
- 47 J. Zhou, Z. Xia, M. S. Molokeev, X. Zhang, D. Peng and Q. Liu, J. Mater. Chem. A, 2017, 5, 15031-15037.
- 48 S. C. Angshuman Nag and D. D. Sarma, J. Am. Chem. Soc., 2008, 130, 10605-10611.
- 49 S. Liu, Z. Wang, H. Cai, Z. Song and Q. Liu, Inorg. Chem. Front., 2020, 7, 1467-1473.
- 50 G. Liu, M. S. Molokeev, B. Lei and Z. Xia, J. Mater. Chem. C, 2020, 8, 9322-9328.
- 51 H. Xia, J. Wang, H. Wang, J. Zhang, Y. Zhang and T. Xu, Rare Met., 2006, 25, 51-57.
- 52 A. Lever, The Crystal Field Splitting Parameter Dq: Calculation and Significance, Werner Centennial, 1967.
- 53 H. Fu, S. Cui, Q. Luo, X. Qiao, X. Fan and X. Zhang, J. Non-Cryst. Solids, 2012, 358, 1217-1220.
- 54 B. Bai, P. Dang, Z. Zhu, H. Lian and J. Lin, J. Mater. Chem. C, 2020, 8, 11760-11770.
- 55 Z. Wang, W. Ye, I.-H. Chu and S. P. Ong, Chem. Mater., 2016, 28, 8622-8630.
- 56 K. Li, M. Shang, Y. Zhang, J. Fan, H. Lian and J. Lin, J. Mater. Chem. C, 2015, 3, 7096-7104.
- 57 H. Zhang, J. Yao, K. Zhou, Y. Yang and H. Fu, Chem. Mater., 2022, 34, 1854-1861.
- 58 S. Sarang, W. Delmas, S. Bonabi Naghadeh, V. Cherrette, J. Z. Zhang and S. Ghosh, J. Phys. Chem. Lett., 2020, 11, 10368-10374.
- 59 Y. Wei, L. Cao, L. Lv, G. Li, J. Hao, J. Gao, C. Su, C. C. Lin, H. S. Jang, P. Dang and J. Lin, Chem. Mater., 2018, 30, 2389-2399.
- 60 Q.-Q. Zhu, L. Wang, N. Hirosaki, L. Y. Hao, X. Xu and R.-J. Xie, Chem. Mater., 2016, 28, 4829-4839.
- 61 D. Wu, L. Liu, H. Liang, H. Duan, W. Nie, J. Wang, J. Peng and X. Ye, Ceram. Int., 2022, 48, 387-396.
- 62 L. You, R. Tian, T. Zhou and R.-J. Xie, Chem. Eng. J., 2021, 417, 129224.
- 63 X. Yuan, S. Ji, M. C. De Siena, L. Fei, Z. Zhao, Y. Wang, H. Li, J. Zhao and D. R. Gamelin, Chem. Mater., 2017, 29, 8003-8011.
- 64 T. Si, Q. Zhu, T. Zhang, X. Sun and J.-G. Li, Chem. Eng. J., 2021, 426, 131744.